NOTES AND CORRESPONDENCE

Airborne Doppler Radar Analysis of a TOGA COARE Waterspout Storm

JOHANNES VERLINDE

Department of Meteorology, The Pennsylvania State University, University Park, Pennsylvania

25 November 1996 and 17 March 1997

ABSTRACT

An airborne Doppler radar analysis of a waterspout parent storm is presented. An 8-min window centered around the time of the visual observation of the waterspout is presented. The waterspout was associated with a small, intense cloud that developed ahead of a squall line. It was observed by radar from a distance of 3 km, with a cross-beam resolution of approximately 70 m. One radar scan cut through the vortex, revealing the structure. The high-resolution dual-Doppler analysis of the Electra Doppler radar was used to investigate the velocity and vorticity structure of the parent storm. These observations were consistent with a low-level vorticity source. No cloud-scale vorticity was observed until the time of the visual observation of the storm.

1. Introduction

Observations of waterspouts and their parent storms with modern observational facilities are rare, in part because they occur over the ocean, away from the dense observational networks over continents, and also because of the small size of these phenomena. Waterspouts may form in rather benign synoptic conditions (Hurd 1950; Brooks 1951; Price and Sasaki 1963), but they can also develop in association with intense squall lines and supercell thunderstorms. Early observational studies relied mostly on visual observations of the funnels themselves (Golden 1968, 1973, 1974a,b, 1977) or conventional radar (Harger and Warden 1962; Golden 1974b). Later studies sought to understand the relationship between the internal cloud-scale circulations and the waterspout using numerical models (Simpson et al. 1986; Simpson et al. 1991). Only recently have waterspout parent storms been observed by Doppler radar, which allowed for some inferences to be drawn about the motions within the parent storm (Golden and Sabones 1991; Wakimoto and Lew 1993), but no dual-Doppler analyses have been reported in the literature.

This paper presents single- and dual-Doppler radar analyses of a waterspout parent storm observed on 10 February 1993 by the National Oceanic and Atmospheric Administration (NOAA) P-3 and the National Center for Atmospheric Research (NCAR) Electra Doppler radar (ELDORA) airborne Doppler radars during the Tropical Oceans Global Atmosphere Coupled Ocean–Atmosphere Response Experiment (TOGA COARE). The ELDORA dataset provided an opportunity to perform a dual-Doppler analysis of the waterspout parent storm approximately 4 min after observers in the NOAA P-3 reported the presence of an ''impressive'' waterspout (B. Smull 1996, personal communication).

This waterspout occurred in the open Pacific Ocean in association with a very intense squall line, which was the focus of the observations. Single-Doppler analyses of two passes by the NOAA P-3 and a dual-Doppler analysis of the ELDORA data are presented. These analyses provide an 8-min window of the evolution of the storm, centered around the time of the visual observation. On its second pass, the NOAA P-3 passed within 3 km of the waterspout, thus providing unprecedented high-resolution observations.

2. Past studies

Waterspouts develop from rapidly growing convective clouds (Golden 1971, 1974a,b; Simpson et al. 1986; Simpson et al. 1991; Wakimoto and Lew 1993) in environments characterized by weak tropospheric wind shears, weak dynamic forcing, and moderate conditional instability. Surface mesoscale boundaries were found to be an essential ingredient in all these cases. Waterspouts are typically located at or near the intersection of colliding boundaries and are associated with a rapid increase in parent storm cloud-top height. Similarities between nonsupercell (no mesocyclone) tornadoes and waterspouts have been documented by Brady and Szoke

Corresponding author address: Hans Verlinde, Department of Meteorology, The Pennsylvania State University, 503 Walker Building, University Park, PA 16802-5013.
E-mail: verlinde@essc.psu.edu

(1989) and Wakimoto and Wilson (1989; hereafter WW89).

Several studies of nonsupercell tornadoes have pointed to the role played by surface features such as gust fronts (Wilson 1986; Simpson et al. 1986; Simpson et al. 1991; WW89; Brady and Szoke 1989). WW89 suggested that gust fronts provide low-level concentrations of vorticity that are sufficient for the generation of all but very intense tornadoes. Golden (1974a), based on visual observations, suggested a similar sequence for waterspout formation in a case he analyzed: individual shower outflows in a squall line acted to concentrate weak large-scale vorticity into the inflow region of the developing cumulus cloud, where it was further concentrated through vertical stretching. Simpson et al. (1986) and Simpson et al. (1991, hereafter S86 and S91) argued that waterspouts are associated with strong cumulus-scale vortex cores that extend all the way down to the surface. They suggested that the role of the gust fronts is to modify the environment in such a way as to force the development of these strong cloud-scale vortices and, further, to intensify occasional cumulus vortices to waterspout intensity. Thus, two hypotheses, differing in the primary source of the original vorticity, have been advanced in the literature. These two hypotheses will be evaluated using the observations collected during the waterspout storm.

3. Data sources and methods of analysis

The NOAA P-3 and the NCAR Electra are the primary data sources for this study. The characteristics of the NOAA P-3 airborne Doppler radar are given by Jorgensen et al. (1983). There is a vertically scanning, X-band (3.2-cm wavelength) Doppler radar mounted in the tail of the aircraft. During TOGA COARE, data were collected using the fore–aft scanning technique (Jorgenson and Smull 1993; Jorgenson et al. 1996), where the antenna was pointing approximately 25° forward from a plane normal to the flight track for one revolution and then turned, pointing aft approximately 25° for the following revolution. By rotating the antenna at its maximum rate of 60° s^{-1} and confining the scanning to one side of the track, a horizontal datum spacing of approximately 750 m was realized for typical P-3 groundspeeds. Radial data spacing is 150 m. Also relevant for this study are the pulse length (0.5 μs, or 150 m), beamwidth (1.35° horizontal and 1.9° vertical), and unambiguous velocity (12.9 m s^{-1}). The aircraft was approximately 3 km from the waterspout; this translates to a half-power beam width horizontal cross section of 70 m.

The waterspout parent storm was located very close to a turning point of the P-3. It was fully observed with the fore scan. However, when the aft scans dissected the storm, the aircraft was already in full turn, hence no useful information could be obtained. Similarly, the fore scan quickly swept through the storm on the return track while the aircraft was still straightening out, but the aft scan provided full coverage. Therefore, it was not possible to use P-3 data to do dual-Doppler analyses.

The P-3 data were carefully edited by looking at all radials. Individual sweeps were subsequently analyzed subjectively. To obtain horizontal cross sections of the storm, data from several sweeps were interpolated onto constant height levels before analysis. These data were not interpolated onto a fixed grid; rather, due to the way these data were collected and the nature of the phenomenon being studied, all points within 100 m vertically from the constant height level were projected onto the horizontal grid level. This resulted, for the horizontal cross sections, in high-resolution (approximately 150 m) datum spacing along the line of interception between the antenna sweep and the constant height analysis planes, but lower (approximately 750 m) datum spacing perpendicular to those lines. The vertical cross sections had very high (less than or equal to 150 m) resolution in all directions.

The NCAR Electra, equipped with the ELDORA, observed the storm 4 min after the second P-3 pass. The operating characteristics of ELDORA during TOGA COARE have been reported by Hildebrand et al. (1996). The 72° s^{-1} rotation rate of the antenna provided approximately 600-m horizontal datum spacing along the flight track with 150-m datum spacing along each radial. These data were interpolated to a Cartesian grid that measured 48 km × 45 km × 18 km (x, y, z) and had a gridpoint spacing of 0.75 km × 0.75 km × 0.5 km. These data were analyzed in the same manner as by Hildebrand et al. (1996). Horizontal velocities were smoothed using a two-step, five-point filter (Leise 1981), retaining wavelengths longer than 4.5 km at 80% of amplitude while eliminating wavelengths shorter than 2.5 km. A storm motion of 11.3 m s^{-1} from 227° was determined for the waterspout storm from a series of NOAA P-3 lower fuselage radar images. This storm motion is subtracted from all the velocities in the dual-Doppler analysis to present the final velocities as storm relative. This storm motion is different from the squall line motion, which was determined to be 7 m s^{-1} from 176° (E. Zipser 1996, personal communication). All the radar data are presented in a common frame of reference with the origin at 6.97°S, 160.16°E.

A composite environmental sounding representative of the squall line inflow was constructed (by M. LeMone of NCAR and E. Zipser of Texas A&M University) of the observations of three aircraft that sampled the area just ahead of the squall line at about 2240–2250 UTC. At higher levels, the sounding is a combination of the best National Aeronautics and Space Administration (NASA) DC-8 dropsondes and flight level data and, higher than that, one of the not-so-nearby ships (E. Zipser 1996, personal communication).

4. System overview

Figure 1 shows a composite reflectivity map for 2308 UTC from the lower fuselage radar in the NOAA P-3.

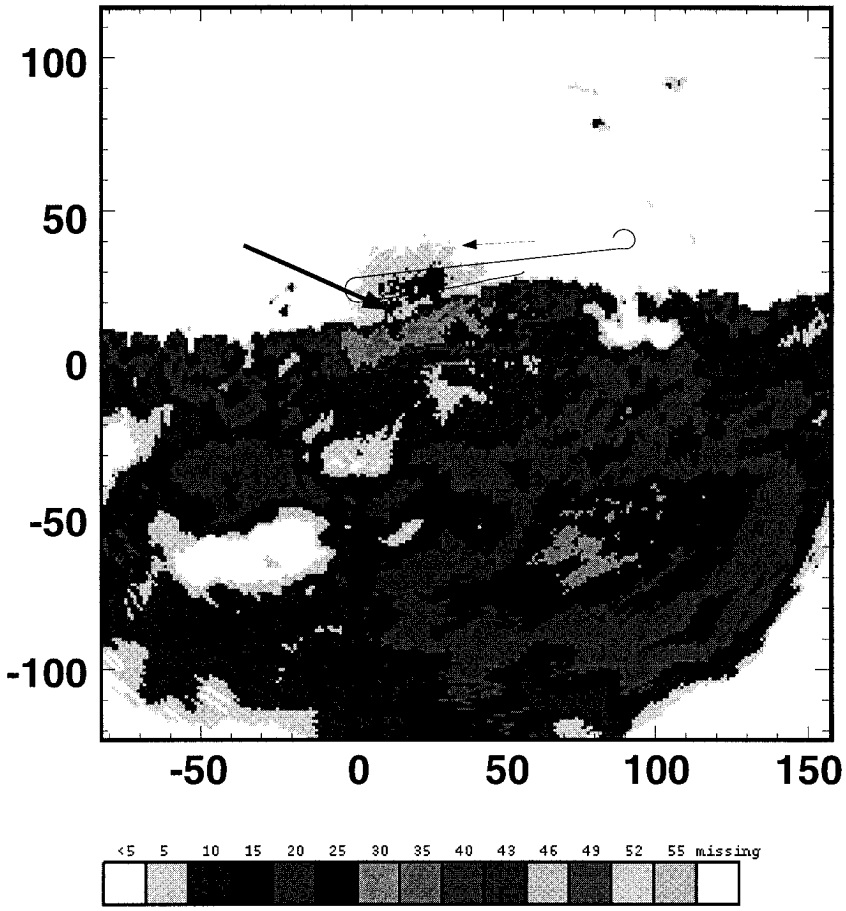

FIG. 1. Composite reflectivity maps constructed from the NOAA P-3 lower fuselage radar data for 2308 UTC. This represents the precipitation structure 6 min before the first detailed analysis. The P-3 flight track and direction are indicated, and the dark arrow indicates the location where the waterspout storm develops.

This composite was constructed from three complete sweeps of the radar, encompassing 2 min of data. The P-3 flight track is superposed on it. The small arrow indicates the direction in which the aircraft was flying, while the heavy arrow indicates the location of the storm. This figure shows an intense squall line with a large trailing stratiform region, with the waterspout storm developing ahead of the main line. On its initial pass, the P-3 passed approximately 15 km to the north of the waterspout storm, but it then turned south and did a second pass approximately 3 km from the storm. During this second pass, the plane encountered a strong gust front at approximately 330 m above mean sea level. An equivalent potential temperature drop of 10 K and winds gusting to 19 m s^{-1} were observed during the penetration of this gust front. Observers on the plane reported a sighting of an ''impressive'' waterspout immediately north of the very intense cell in the leading edge of the line. Unfortunately, the aircraft was still coming out of its turn, and the observers lost sight of it before any pictures could be taken (B. Smull 1996, personal communication).

The sounding (Fig. 2a) reveals an unstable subcloud layer, with the lifting condensation level near the weak inversion at 950 hPa. The air above the inversion layer is characterized by a series of shallow, conditionally unstable layers overlaid by absolutely stable layers up to approximately 660 hPa (3.6 km). Only a small amount of the convective available potential energy (CAPE) was found in this layer. Most of the environmental CAPE was present in the conditionally unstable layer above 660 hPa. The total CAPE of the sounding was 1730 J kg^{-1}. The hodograph (Fig. 2b) reveals significant shear (7.2×10^{-3} s^{-1}) in the layer just above cloud base (958 hPa, 450 m) to 850 hPa (1500 m), then weaker shear up to 728 hPa (2800 m), and then another stronger shear layer (8.3×10^{-3} s^{-1}) up to 600 mb.

Figures 3 and 4 show analyses of the two passes by the NOAA P-3. Data locations (the sweep lines in the analysis plane) are indicated in the upper left panel in

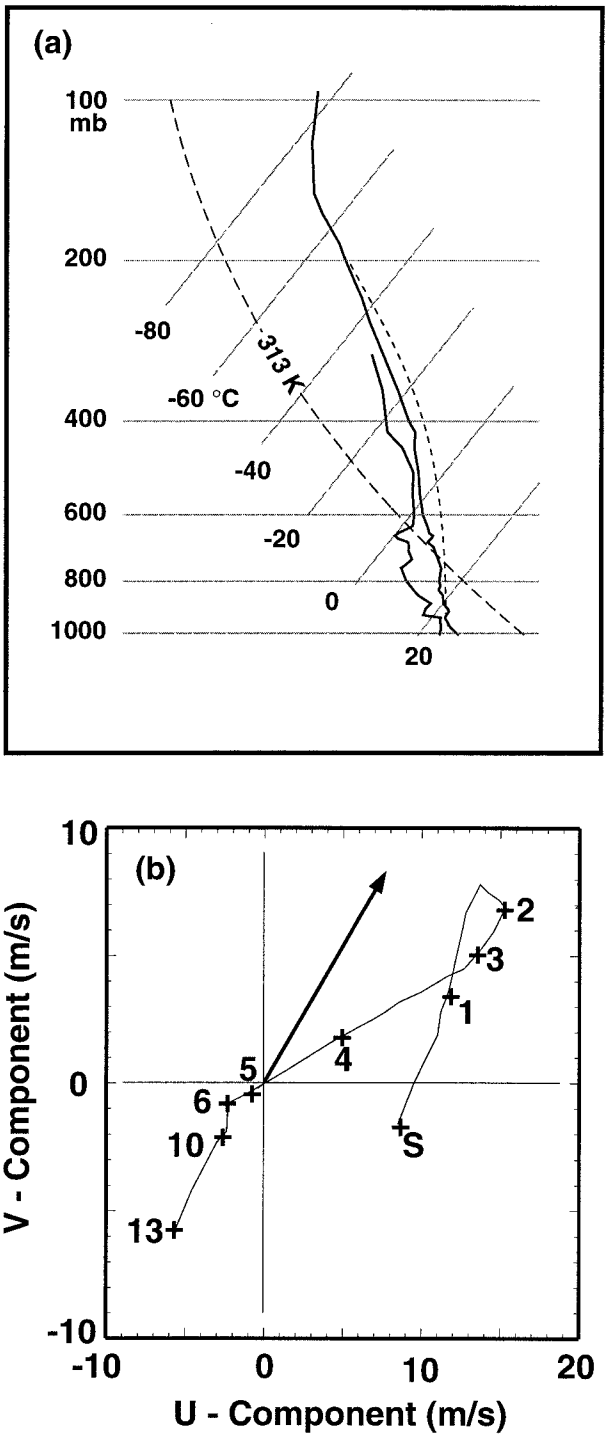

FIG. 2. The (a) environmental sounding and (b) hodograph. A lifted surface parcel is indicated.

both figures. Further, lines perpendicular to the sweep line are shown in the two right-hand top panels in Fig. 4.

Very careful attention was given to the editing of the radial velocity data. For example, data from the cross section through the core of the waterspout storm are presented in Tables 1 (radial velocities) and 2 (reflectivities) for a section of one sweep from the second P-3 pass. Of particular interest are those radial velocities in boldface print. Since the Nyquist interval is 25.8 m s^{-1}, these points could be either in the -10–0 m s^{-1} or 15–25 m s^{-1} range. An analysis of the full sweep (see Fig. 4) reveals that these velocities are in the inflow (updraft) region of the cloud. Projecting the environmental winds onto a radial only yielded marginally negative values, giving support to the positive range of velocities. Evaluation of the surrounding velocities reveals a strong along-beam gradient (approximately 15 m s^{-1} over 150 m) from high to low velocities. This gradient is slightly weaker than that estimated by Golden (1974b) for a Florida Keys waterspout, although here the gradient is constrained by the datum spacing. With the closely collocated high reflectivities, which could be the result of seaspray interacting with cloudy air, the conclusion was reached that this sweep of the P-3 radar cut through the waterspout vortex.

Figure 3 presents results from the analysis of the 2314 UTC pass scans. The top panels are horizontal cross sections at 2 km. The lower four panels represent vertical cross sections (reflectivity and radial velocity) along the sweep lines indicated by A (left-hand lower two panels) and B (right-hand lower two panels). The 30-dB*Z* contour in the horizontal cross section bulges out toward the front of the system in an anchor-like appendage. The weak-echo regions (WERs) separating the hooks of the anchor from the intense (50+ dB*Z*) echoes behind are also associated with low-magnitude positive or negative values (away from the radar) of radial velocities, indicative of an updraft region of the cloud, since the low-level environmental winds have only a small component when projected onto a radial. The vertical cross sections through these WERs are even more revealing. A WER is clearly evident in both. This WER lines up well with the low positive–negative radial velocity region. It is clear that the 50-dB*Z* values are associated with this developing storm, and not the squall line, which is approximately another 5 km behind. Note that although the storm has 50+ dB*Z* echoes, its echo top at this instance barely exceeds 4 km. These high reflectivities are probably indicative of a very efficient warm-cloud precipitation process.

The structure revealed in Fig. 3 suggests a storm with a strong updraft, overturning at the top, where it is working against the stable environmental layer shown in Fig. 2. The structure is very reminiscent of the structure of a severe midlatitude storm (Browning and Ludlam 1962); however, this resembles only a miniature version of it. At this stage of the storm's life cycle, the observations reveal little indication of any cumulus-scale vortices throughout the depth of the cloud.

Figure 4 presents results from the analysis of the 2318 UTC pass scans. The P-3 had made its turn and was now within a few kilometers of the waterspout storm. Observers noted the waterspout moments before these

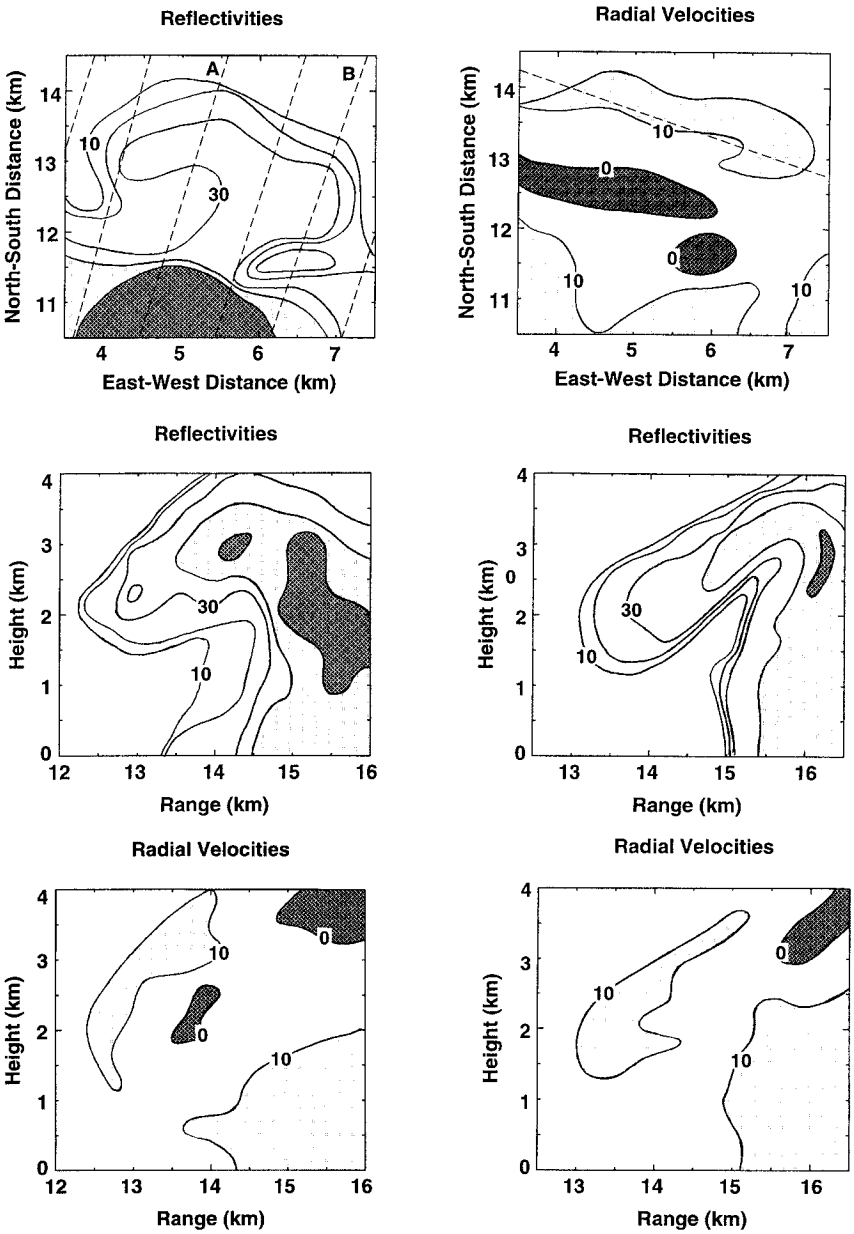

FIG. 3. Analysis of the P-3 data for the 2314 UTC pass. The top panels are horizontal cross sections at 2 km of reflectivity and radial velocity. Radials are indicated by the light dashed lines in the reflectivity plot. The lower panels are vertical cross sections of reflectivity and radial velocity through radial A (left-hand two panels) and radial B (right-hand two panels). The horizontal cross sections are presented in distances north and east of the origin (see text), while the vertical cross sections are presented in height above the surface vs range from the aircraft. Positive radial velocities are toward the aircraft.

observations. The top four panels in this figure are horizontal cross sections: the top two at 1.5 km and the middle two at 2 km. The lowest two panels in the figure are analyses of the vertical cross section through the sweep labeled A in the top left panel.

There is still evidence of the WER in the reflectivity fields at 2 km, even though it has filled in significantly since the previous pass. The WER is much more pronounced at 1.5 km where the reflectivity fields reveal a hook-echo structure, similar to that frequently seen in association with tornadic storms in midlatitudes (Browning and Ludlam 1962). There is also an interesting high-reflectivity maximum, with an associated radial velocity maximum, centered in the WER. As in Fig. 3, the WER is primarily characterized by low positive or negative radial velocities, indicative of the up-

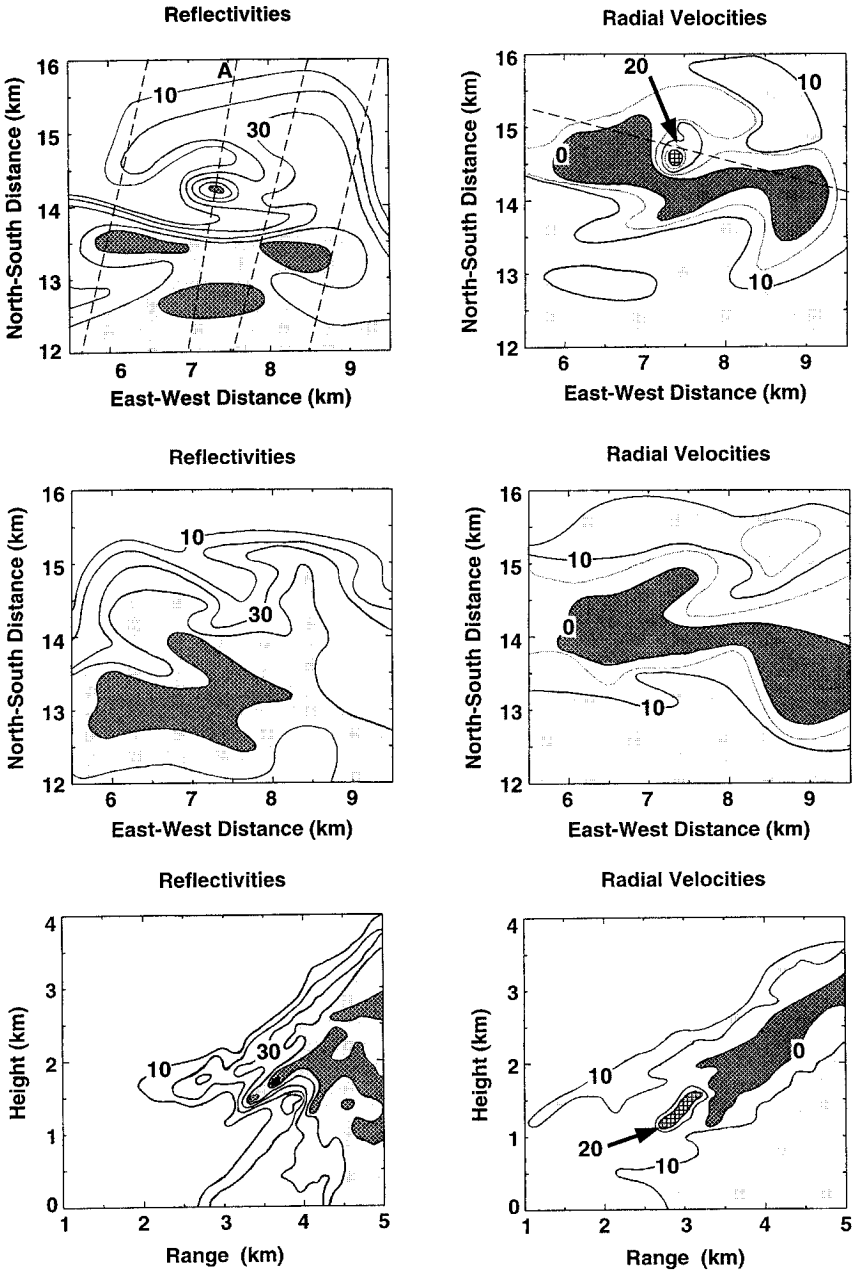

FIG. 4. Analysis of the P-3 data for the 2318 UTC pass. The top four panels are horizontal cross sections of reflectivity and radial velocity at 1.5 km (top two) and 2 km (center two) altitude. The light dashed lines in the velocity plots represent plane perpendicular to the scanning plane. The bottom two panels are vertical cross sections of reflectivity and radial velocity through radial A. The horizontal cross sections are presented in distances north and east of the origin (see text), while the vertical cross sections are presented in height above the surface vs range from the aircraft. Positive radial velocities are toward the aircraft.

draft. Only in a very small spot (two bins across or 300 m) does one see the 20+ m s^{-1} velocities that were the subject of discussion associated with Table 1. There is a slight offset between the regions of high reflectivity and high radial velocities. The radial-to-radial shear (the equivalent of what for a ground-based radar would be the azimuthal shear) along the dashed line in the top right-hand panel is 27×10^{-3} s^{-1}, meeting the WW89 criterion for a tornado vortex signature (TVS; Brown et al. 1978). The radial velocities at 2 km (center right-hand panel) indicate a (Southern Hemisphere) anticyclonic circulation above this feature.

The vertical cross sections give further insight into this high-reflectivity–high-radial velocity couplet in the

TABLE 1. Detailed radial velocities for cut through waterspout. Here azimuth refers to the pointing angle of the antenna in the sweep plane.

	Azimuth														
Range	77.84	76.92	75.62	74.53	73.43	72.15	70.96	69.78	68.59	67.41	66.32	65.30	63.88	62.80	61.72
2.100															17.5
2.250														5.6	8.0
2.400											8.4	3.4	4.1	3.4	1.2
2.550							4.2	7.6	4.6	5.5	5.0	5.7	8.7	4.2	5.9
2.700			**23.0**	9.2	**21.2**	**22.5**	**24.6**	3.9	1.0	4.5	3.3	2.1	10.1	4.5	6.4
2.850	7.0	4.0	**15.1**	**23.3**	4.4	**23.5**	1.4	**23.7**	3.7	**22.4**	5.3	0.2	6.3	1.7	5.3
3.000	15.4	5.5	0.5	4.0	2.7	16.7	0.8	**18.7**	**19.3**	**18.0**	**22.4**	2.1	**14.9**	1.4	5.1
3.150	12.2	13.5	8.5	3.6	3.6	1.5	4.0	1.9	5.0	**20.8**	2.0	1.0	6.9	3.4	4.5
3.300	14.7	6.3	−2.3	0.0	−0.9	−0.9	0.4	−2.0	4.5	4.1	0.9	−1.2	−0.5	3.4	6.9
3.450	14.3	11.6	5.5	2.8	1.7	0.5	0.7	−2.0	2.3	1.6	1.2	−2.2	4.7	−2.0	3.7
3.600	10.6	9.3	−0.9	6.6	7.5	1.4	2.2	−2.1	3.1	1.5	−0.8	−4.8	2.9	−1.6	2.7
3.750	10.6	9.5	3.1	5.5	2.5	−4.7	3.0	−6.3	−1.0	−2.7	−1.6	−1.5	−0.5	−1.2	0.9
3.900	11.1	12.4	10.1	11.8	9.5	0.9	3.0	0.3	−2.9	−4.5	−1.8	−3.6	3.5	−3.4	1.6
4.050	11.1	13.5	9.3	11.5	12.7	0.6	4.7	1.7	6.1	−2.3	−2.3	−6.2	0.1	−2.0	1.3
4.200	14.3	14.1	8.7	10.3	10.9	17.9	8.2	4.1	6.7	4.5	−0.3	0.4	4.3	−3.7	0.3
4.350	12.8	11.9	4.9	11.9	14.7	10.6	11.2	10.3	8.6	14.4	3.7	−1.2	12.8	−3.4	0.5
4.500	14.4	13.7	8.7	13.9	14.5	9.9	12.8	8.9	9.4	11.2	8.0	10.1	9.6	6.8	4.4
4.650	17.5	13.6	5.2	15.0	12.3	11.1	13.6	11.2	8.5	7.2	4.5	3.3	14.1	2.6	2.8
4.800	16.7	15.9	8.0	13.5	13.1	10.3	12.4	12.1	13.3	5.3	5.4	12.6	16.1	1.4	3.9
4.950	15.6	15.1	10.3	13.6	14.5	11.1	14.0	11.5	10.2	12.0	8.8	8.6	11.7	4.9	4.9
5.100	16.8	17.7	8.7	14.0	13.2	11.7	15.0	10.5	10.3	13.5	10.2	8.9	17.9	11.3	6.7

WER. Both features are revealed as narrow structures, leaning into the storm. They are aligned with the radial velocity peak approximately 300 m ahead and above the high-reflectivity feature, apparently at the front edge of the updraft. (See the 1.5 km velocities, presented in the top left-hand panel of the figure.) The velocity peak lies in the center of a low-reflectivity notch extending up to about 2.2 km in the cloud. Wakimoto et al. (1996) observed a similar feature in Verification of the Origin of Rotation in Tornadoes Experiment tornadoes.

At this stage the cloud top was approximately 5 km. The updraft evidently had broken through the stable lower layers in the sounding, and the cloud top was now growing in the unstable region.

Yet 4 min later, at 2322 UTC, the NCAR Electra passed this storm, observing it with the ELDORA. Figures 5 and 6 show some analyses from this dataset. The X-band radar signal suffered significant attenuation going through the intense leading cells, resulting in some irregular features toward the south of (behind) the lead-

TABLE 2. Detailed reflectivity value for cut through waterspout. Here azimuth refers to the pointing angle of the antenna in the sweep plane.

	Azimuth														
Range	77.84	76.92	75.62	74.53	73.43	72.15	70.96	69.78	68.59	67.41	66.32	65.30	63.88	62.80	61.72
2.100															0.0
2.250														0.0	3.0
2.400											0.0	0.0	0.0	8.0	12.0
2.550							0.0	0.0	0.0	5.0	16.0	13.0	25.0	25.0	20.0
2.700			0.0	0.0	0.0	0.0	0.0	0.0	0.0	1.0	15.0	15.0	25.0	23.0	24.0
2.850	0.0	0.0	0.0	0.0	0.0	0.0	0.0	0.0	0.0	0.0	6.0	16.0	19.0	19.0	24.0
3.000	0.0	0.0	8.0	14.0	5.0	0.0	0.0	0.0	2.0	6.0	9.0	20.0	24.0	24.0	30.0
3.150	1.0	0.0	0.0	7.0	16.0	23.0	29.0	26.0	25.0	13.0	16.0	18.0	23.0	32.0	33.0
3.300	6.0	2.0	0.0	6.0	13.0	29.0	41.0	52.0	47.0	38.0	30.0	26.0	25.0	34.0	35.0
3.450	12.0	4.0	2.0	2.0	7.0	15.0	33.0	49.0	49.0	45.0	39.0	32.0	28.0	35.0	39.0
3.600	15.0	17.0	18.0	16.0	16.0	10.0	20.0	36.0	53.0	60.0	46.0	41.0	31.0	34.0	37.0
3.750	17.0	17.0	9.0	7.0	9.0	7.0	10.0	28.0	42.0	51.0	50.0	45.0	36.0	32.0	31.0
3.900	31.0	32.0	25.0	16.0	8.0	13.0	20.0	34.0	39.0	48.0	50.0	52.0	42.0	39.0	36.0
4.050	35.0	50.0	54.0	51.0	40.0	30.0	36.0	43.0	54.0	57.0	55.0	50.0	43.0	44.0	45.0
4.200	38.0	40.0	45.0	49.0	53.0	54.0	53.0	57.0	55.0	55.0	52.0	56.0	54.0	42.0	42.0
4.350	45.0	38.0	43.0	40.0	47.0	52.0	58.0	51.0	55.0	47.0	52.0	56.0	58.0	53.0	51.0
4.500	49.0	52.0	48.0	43.0	49.0	46.0	55.0	51.0	54.0	46.0	49.0	47.0	50.0	46.0	45.0
4.650	45.0	44.0	49.0	52.0	57.0	50.0	47.0	50.0	50.0	51.0	50.0	46.0	49.0	48.0	46.0
4.800	52.0	48.0	53.0	53.0	54.0	48.0	54.0	45.0	49.0	47.0	48.0	50.0	48.0	45.0	53.0
4.950	45.0	51.0	45.0	50.0	48.0	49.0	47.0	50.0	46.0	48.0	45.0	43.0	44.0	54.0	54.0
5.100	38.0	44.0	48.0	51.0	49.0	50.0	41.0	40.0	43.0	41.0	40.0	49.0	46.0	54.0	53.0

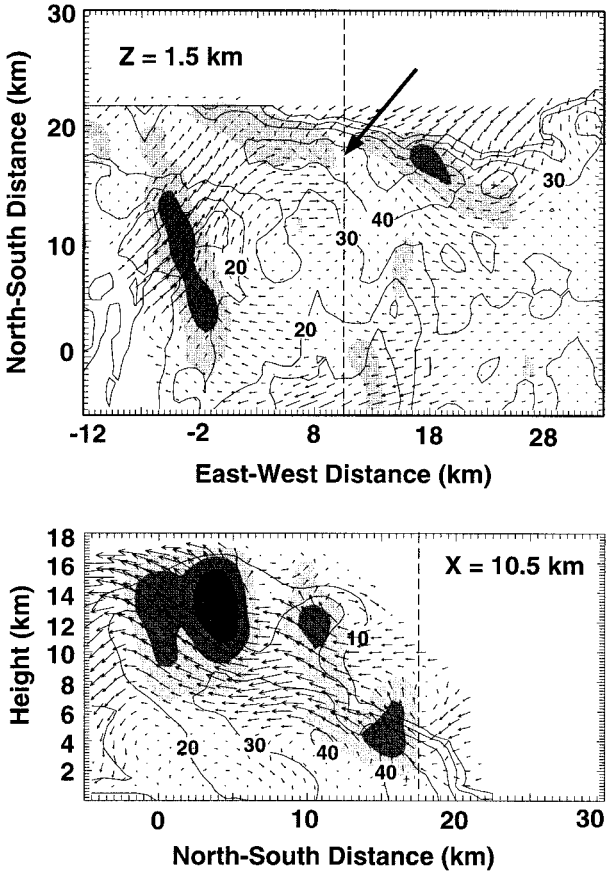

FIG. 5. (a) The 1.5-km altitude horizontal (vectors) and vertical (shading) winds and reflectivity (contours) from the ELDORA dual-Doppler analysis. (b) Vertical cross section through the center of the vortex. Reflectivity contours are at every 10 dBZ beginning at 10 dBZ. Vertical velocity shadings at 5 m s^{-1} intervals beginning at 2.5 m s^{-1}. The magnitude of a 10 m s^{-1} vector is indicated in the top panel. The arrow in the top panel points to the center of the circulation.

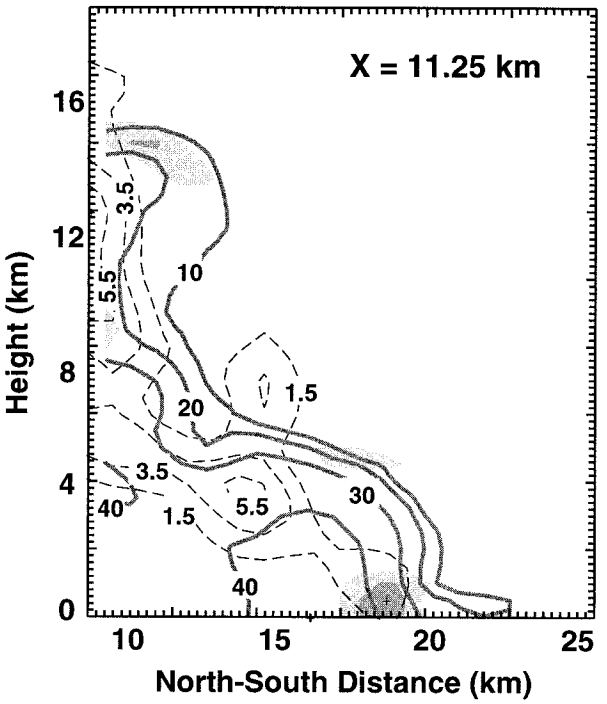

FIG. 6. Vertical cross section of reflectivity (light gray contours), vertical velocity (thin dashed contours), and positive vorticity (shading) through the highest vorticity location. Reflectivity contours are at every 10 dBZ beginning at 10 dBZ. Vertical velocity contours are at every 2 m s^{-1} beginning at 1.5 m s^{-1}. Vorticity shading is at 3×10^{-3} s^{-1} intervals beginning at 4×10^{-3} s^{-1}.

ing line. Vertical cross sections from individual sweeps showed little indication of the strong overhangs observed in the P-3 passes; however, this is not inconsistent with the P-3 observations, since the WER became less prominent going from 2314 to 2318 UTC.

The dual-Doppler analysis from the ELDORA confirmed the observers' comments that this was a very intense tropical squall line. Vertical velocities up to 23 m s^{-1} were analyzed in the main line. The vertical velocity profile had dual-altitude peaks: the lower altitude peak between 3 and 7 km, and the higher between 10 and 16 km. This bimodal feature has been observed by other researchers as well (Hildebrand et al. 1996; Trier et al. 1996).

Figure 5 shows horizontal and vertical cross sections through the waterspout parent storm. Velocity vectors are presented in storm-relative coordinates. A prominent anticyclonic circulation (indicated by the arrow) can be seen in the 1.5-km height horizontal cross section. The location coincides with the projected location of the P-3 WER using the derived storm motion. This circulation is associated with the horizontal wind shear line between the squall line outflow and the environmental flow. The circulation is clearly distinguishable at lower altitudes but becomes weaker higher in the cloud (Fig. 6). It is located between two vertical velocity peaks at 1 km (vertical velocities greater than 2.5 m s^{-1} are indicated by the shaded region). The maximum vorticity value determined in this analysis was 7.2×10^{-3} s^{-1}, which is well within the range of midlatitude mesocyclone values.

The vertical cross section was taken along the dashed line through the center of the circulation. Three active convective regions, all in different stages of development, can be discerned. The circulation (its position indicated by the dashed line) is associated with an actively growing cell ahead of the other two more mature cells. The latter two cells were part of the greater squall line. The circulation is associated with the fast-growing smaller cell, where it was present mostly at the edge of the main updraft. This analysis lends support to the conclusions of the structure of the storm drawn from the single-Doppler analyses.

At this stage the waterspout storm was growing rapidly in a favorable environment. The 10-dB*Z* echo top had grown through the 6-km height level. An approximation of the vertical growth rate of the 10-dB*Z* echo

TABLE 3. Analysis of the vorticity terms in the 1-km² area around the vorticity maximum.

Height (km)	Average vorticity ($\times 10^{-3}$ s^{-1})	Advection (Hor) ($\times 10^{-6}$ s^{-1})	Advection (Ver) ($\times 10^{-6}$ s^{-1})	Stretching ($\times 10^{-6}$ s^{-1})	Tilting ($\times 10^{-6}$ s^{-1})
0.0	6.0	1.6	—	17.4	—
0.5	6.1	4.8	0.8	19.5	0.3
1.0	5.5	1.8	6.7	17.0	0.8
1.5	3.1	6.3	11.6	6.4	1.4
2.0	3.4	0.6	−0.9	8.9	−1.0
2.5	3.3	2.8	5.5	10.0	2.6

top altitude was determined from the 2314 and 2322 UTC analyses to be 8 m s^{-1}. Vertical velocities up to 16 m s^{-1} were found in this storm.

Figure 6 shows a vertical cross section through the storm along the 1-km height vorticity maximum. It reveals that the significant anticyclonic vorticity (defined to be 4×10^{-3} s^{-1}) is confined to the lower 2 km of the cloud, below and slightly ahead of the main updraft region of the cloud.

The equation for the vertical component of vorticity can be written as

$$\frac{\partial \zeta}{\partial t} = \underbrace{-\left(u\frac{\partial \zeta}{\partial x} + v\frac{\partial \zeta}{\partial y}\right)}_{\text{A}} \underbrace{- w\frac{\partial \zeta}{\partial z}}_{\text{B}} \underbrace{- (\zeta + f)\left(\frac{\partial u}{\partial x} + \frac{\partial v}{\partial y}\right)}_{\text{C}} \underbrace{- \left(\frac{\partial w}{\partial x}\frac{\partial v}{\partial z} - \frac{\partial w}{\partial y}\frac{\partial u}{\partial z}\right)}_{\text{D}} + \underbrace{\frac{1}{\rho^2}\left(\frac{\partial \rho}{\partial x}\frac{\partial p}{\partial y} - \frac{\partial \rho}{\partial y}\frac{\partial p}{\partial x}\right)}_{\text{E}} + \underbrace{\left(\frac{\partial F_y}{\partial x} - \frac{\partial F_x}{\partial y}\right)}_{\text{F}}, \quad (1)$$

where u, v, and w are the components of the observed winds; ρ is the density; p is the pressure; ζ is the vertical component of vorticity; and F_x and F_y are the subgrid-scale forces. Here, A and B are the horizontal and vertical advection of vorticity, respectively; while C, D, E, and F are the stretching, tilting, solenoidal, and subgrid-scale generation terms, respectively. Terms A, B, C, and D have been calculated from the dual-Doppler analysis. Here F typically is much smaller than the other terms (Verlinde and Cotton 1990), and E requires knowledge about the mass fields that is not available from the dual-Doppler analysis. Average values for A, B, C, and D were calculated from the nine grid points centered over the location of maximum vorticity. The results are presented in Table 3. The stretching term clearly dominates the calculated terms at lower levels, while the contribution of the tilting term is negligible.

5. Discussion

The observations presented are more consistent with the WW89 than the S86 and S91 hypothesis for the formation of waterspouts. The observations indicate that, at least in some waterspout storms, the source of vorticity is primarily in the lower levels in association with the surface gust front, independent of a cumulus-scale circulation. This conclusion is supported by the time series of observations at 2 km, where the first indication of significant vorticity was observed only after the waterspout was already under way. The analysis prior to that time revealed only weak vorticity, if any. Further, the sharp drop off with height of the vorticity is associated with the circulation point toward a low-level source of vorticity resulting from the horizontal shear between the gust front and the environmental winds rather than from the vertical shear of the horizontal wind. The evaluation of the vertical vorticity equation forcing terms also supports this view. The stretching term dominates the other calculated source terms. The small tilting term would seem to indicate that the vertical shear of the horizontal wind did not play a significant role in the formation of the circulation.

An analysis of the radar-observed fields of a sweep through the waterspout was also presented. Radial velocities up to 25 m s^{-1} were observed in a narrow, 300-m wide band. This band of high velocities was located ahead of the main updraft core of the storm and in a trough of lower reflectivities, reminiscent of the weak-echo hole associated with severe tornadoes (Wakimoto et al. 1996). Parallel to this band of high velocities, but below it, a band of high reflectivities was observed. There was no indication of a similar band above. These high reflectivities may be the result of seaspray (which had been sucked into the cloud by the waterspout, seeding the cloud) producing an efficient precipitation formation process. The heavier drops are then preferentially located below the vortex.

6. Summary and conclusions

Observations of an intense oceanic convective storm have been presented. This storm developed along the leading gust front of an intense squall line, several kilometers ahead of the main line. Three sets of airborne Doppler data taken during successive passes were used to investigate the evolution of the storm during its early growth period. During the 8 min this storm was observed, the radar storm top height increased from 4 km to higher than 6 km. At this time, the storm was characterized by a strong updraft (shown by the WER), it precipitated heavily (reflectivities in excess of 50 dBZ), and a waterspout was observed. The waterspout was observed by radar from a distance of 3 km, with a cross-beam resolution of approximately 70 m. One radar scan cut through the vortex, revealing the structure.

The high-resolution dual-Doppler analysis of the EL-

DORA radar was used to investigate the velocity and vorticity structure of the parent storm. These observations are more consistent with the WW89 than the S86 and S91 hypothesis for the formation of waterspouts. They point toward a low-level source of vorticity resulting from the horizontal shear between the gust front and the environmental winds rather than from the vertical shear of the horizontal wind.

Acknowledgments. Peter Hildebrand of NCAR/RSF suggested this as a interesting dataset to look at for an assignment in the radar meteorology course I taught at Penn State in the spring of 1995. He also provided help with the analysis of the ELDORA data. Dave Jorgensen provided the P-3 data and his analysis software. Peggy LeMone from NCAR and Ed Zipser from Texas A&M provided their analysis of the squall line inflow sounding. I thank the crews of the NCAR Electra (Peggy LeMone, mission scientist) and the NOAA P-3 (Brad Smull, mission scientist) for collecting the data.

REFERENCES

Brady, R. H., and E. Szoke, 1989: A case study of nonmesocyclone tornado development in northeast Colorado: Similarities to waterspout formation. *Mon. Wea. Rev.,* **117,** 843–856.

Brooks, E. M., 1951: Tornadoes and related phenomena. *Compendium of Meteorology,* T. F. Malone, Ed., Amer. Meteor. Soc., 673–680.

Brown, R. A., L. R. Lemon, and D. W. Burgess, 1978: Tornado detection by pulsed Doppler radar. *Mon. Wea. Rev.,* **106,** 29–38.

Browning, K. A., and F. H. Ludlam, 1962: Airflow in convective storms. *Quart. J. Roy. Meteor. Soc.,* **88,** 117–135.

Golden, J. H., 1968: Waterspouts at Lower Matecumbe Key, Florida, 2 September 1967. *Weather,* **23,** 103–114.

——, 1971: Waterspouts and tornadoes over south Florida. *Mon. Wea. Rev.,* **99,** 146–154.

——, 1973: Some statistical aspects of waterspout formation. *Weatherwise,* **26,** 108–117.

——, 1974a: The life cycle of Florida Keys' waterspouts. I. *J. Appl. Meteor.,* **13,** 676–692.

——, 1974b: Scale-interaction implications for the waterspout life cycle. II. *J. Appl. Meteor.,* **13,** 693–709.

——, 1977: An assessment of waterspout frequencies along the U.S. east and gulf states. *J. Appl. Meteor.,* **16,** 231–236.

——, and M. E. Sabones, 1991: Tornadic waterspout formation near intersecting boundaries. Preprints, *25th Int. Conf. on Radar Meteorology,* Paris, France, Amer. Meteor. Soc., 420–423.

Harger, G., and J. D. Warden, 1962: A radar echo configuration associated with a series of waterspouts. *Mon. Wea. Rev.,* **90,** 197–200.

Hildebrand, P. H., and Coauthors, 1996: The ELDORA/ASTRAIA airborne Doppler weather radar: High-resolution observations from TOGA COARE. *Bull. Amer. Meteor. Soc.,* **77,** 213–232.

Hurd, W. E., 1950: Some phases of waterspout behavior. *Weatherwise,* **3,** 75–82.

Jorgensen, D. P., and B. F. Smull, 1993: Mesovortex circulations seen by airborne Doppler radar within a bow-echo mesoscale convective system. *Bull. Amer. Meteor. Soc.,* **74,** 2146–2156.

——, P. H. Hildebrand, and C. L. Frush, 1983: Feasibility test of an airborne pulse-Doppler meteorological radar. *J. Climate Appl. Meteor.,* **22,** 744–757.

——, T. Matejka, and J. D. DuGranrut, 1996: Multi-beam techniques for deriving wind fields from airborne Doppler radars. *Meteor. Atmos. Phys.,* **59,** 83–104.

Leise, J. A., 1981: A multi-dimensional, scale-telescoped filter and data extension package. NOAA Tech. Memo ERL WPL-82, 24 pp.

Price, S., and R. I. Sasaki, 1963: Some tornadoes, waterspouts, and other funnel clouds of Hawaii. *Mon. Wea. Rev.,* **91,** 175–192.

Simpson, J., B. R. Morton, M. C. McCumber, and R. S. Penc, 1986: Observations and mechanisms of GATE waterspouts. *J. Atmos. Sci.,* **43,** 753–782.

——, C. Roff, B. R. Morton, K. Labas, G. Dietachmayer, M. McCumber, and R. Penc, 1991: A Great Salt Lake waterspout. *Mon. Wea. Rev.,* **119,** 2741–2770.

Trier, S. B., W. C. Skamarock, M. A. LeMone, D. B. Parsons, and D. P. Jorgensen, 1996: Structure and evolution of the 22 February 1993 TOGA COARE squall line: Numerical simulations. *J. Atmos. Sci.,* **53,** 2861–2886.

Verlinde, J., and W. R. Cotton, 1990: A mesoscale vortex couplet observed in the trailing anvil of a multicellular convective complex. *Mon. Wea. Rev.,* **118,** 993–1010.

Wakimoto, R. M., and J. W. Wilson, 1989: Nonsupercell tornadoes. *Mon. Wea. Rev.,* **117,** 1113–1140.

——, and J. K. Lew, 1993: Observations of a Florida waterspout during CaPE. *Wea. Forecasting,* **8,** 412–423.

——, W.-C. Lee, H. B. Bluestein, C.-H. Liu, and P. H. Hildebrand, 1996: ELDORA observations during VORTEX 95. *Bull. Amer. Meteor. Soc.,* **77,** 1465–1481.

Wilson, J. W., 1986: Tornadogenesis by nonprecipitation-induced wind shear lines. *Mon. Wea. Rev.,* **114,** 270–284.